POLITECNICO DI TORINO
Repository ISTITUZIONALE

Assessing the Effect of Stabilization and Carbonization Temperatures on Electrochemical Performance
of Electrospun Carbon Nanofibers from Polyacrylonitrile

(Article begins on next page)

19 April 2024

RESEARCH ARTICLE

ADVANCED
ENERGY & SUSTAINABILITY
RESEARCH
Open Access

www.advenergysustres.com

Assessing the Effect of Stabilization and Carbonization Temperatures on Electrochemical Performance of Electrospun Carbon Nanofibers from Polyacrylonitrile

Felix Boll, Matteo Crisci, Leonardo Merola, Francesco Lamberti, Bernd Smarsly, and Teresa Gatti*

Supercapacitors (SCs) are considered a promising alternative to batteries to power up portable and wearable devices. Among different categories of materials for SCs, carbon nanofibers (CNFs) are particularly appealing for their electrochemical, morphological, and mechanical properties, coupled with the ease of synthesis. Electrospinning is a simple and low-cost technique to prepare the polymer-based precursors for CNFs, allowing to obtain fibers with a tunable morphology and a diameter in the nanometer range. However, even if electrospun CNFs were intensely studied over the years, in the literature there is a lack of information regarding the optimization of the thermal treatment to prepare bare CNFs with high specific capacitance (C_s). Herein, a systematic study on the optimization of the stabilization and carbonization temperatures for electrospun CNFs prepared from polyacrylonirtile is reported, achieving a maximum C_s of 49 F g^{-1} at 0.5 A g^{-1} in a symmetrical SC device based on 1 M H$_2$SO$_4$ electrolyte. Aspects related to the specific surface area, nitrogen doping, and carbon microstructure are examined concerning the different thermal treatments, allowing to define structure–property–function relationships in these capacitive nanoarchitectures.

1. Introduction

Portable and wearable devices will increasingly play a crucial role in our everyday lives. Even if markets for portable and wearable technologies are set to grow tremendously, these devices require an efficient energy storage system (ESS) as a powering source.[1,2] There are different ESS types based on factors such as energy density (E_d), power density (P_d), and operation lifetime. ESSs can be divided into electromechanical, electromagnetic, electrochemical, chemical, and electrostatic.[2] Among all energy storage devices, rechargeable batteries and electrochemical capacitors, also known as supercapacitors (SCs), are the most suitable choices to store energy for portable and wearable devices. SCs are indeed considered valuable alternatives to batteries for these applications because they allow superior durability and an ultrafast charge–discharge time, enabling high P_d.

From a general point of view, electrodes for SCs should have high electrical conductivity, good chemical stability, high specific surface area (SSA) for contact with the electrolyte, resistance to corrosion, and thermal stability. Currently, several different categories of materials can be employed to fabricate an electrode for SCs, such as nanostructured carbon-based materials, conducting polymers, transition metal oxides, or other new emerging categories of materials like metal–organic frameworks (MOFs),[3,4] MXenes,[5] transition metal dichalcogenides, metal nitrides (MNs), and black phosphorus.[6]

Within this list, nanostructured carbon is one of the most studied and developed classes, with the longest history in research. Activated carbon,[7–10] graphene,[11,12] carbon nanotubes,[13–16] carbon aerogels,[17–19] carbon nanofibers (CNFs),[20] and laser-induced graphene[21,22] are some examples of the multitude of carbon-based materials used as scaffold electrodes for SC applications. Between all these different materials

F. Boll, M. Crisci, L. Merola, B. Smarsly
Institute of Physical Chemistry
Justus Liebig University
Heinrich-Buff-Ring 17, 35392 Giessen, Germany

The ORCID identification number(s) for the author(s) of this article can be found under https://doi.org/10.1002/aesr.202300121.

F. Boll, M. Crisci, B. Smarsly, T. Gatti
Center for Materials Research
Justus Liebig University
Heinrich-Buff-Ring 17, 35392 Giessen, Germany

L. Merola, F. Lamberti
Department of Chemical Sciences
University of Padova
via Marzolo 1, 35131 Padova, Italy

T. Gatti
Department of Applied Science and Technology
Politecnico di Torino
Corso Duca degli Abruzzi 24, 10129 Torino, Italy
E-mail: teresa.gatti@polito.it

www.advancedsciencenews.com

**ADVANCED
ENERGY & SUSTAINABILITY
RESEARCH**
Open Access

www.advenergysustres.com

CNFs have attracted the interest of the scientific community due to their relatively high surface area (400–600 m^2 g^{-1}), enabling efficient contact with the electrolyte, high electrical conductivity (1–10^2 S cm^{-1}), tuneable pore size distribution, lack of insulating binder to support the microstructure ease of synthesis process, and relatively low cost of fabrication.[23] CNFs can be easily prepared through electrospinning deposition of polymer-based precursor fibers, which, after a thermal treatment, are converted into CNFs. These polymer-based precursor fibers can be obtained from different polymers, among others, polyacrylonitrile (PAN), polyvinylpyrrolidone (PVP), cellulose acetate (CA), polyvinyl alcohol (PVA), polymethyl methacrylate (PMMA), polyimide (PI), and from different solvents like dimethylsulfoxide (DMSO), dimethylacetamid (DMAc), dimethyl sulfone, and tetramethyl sulfide.[23,24] PAN produces CNFs with the highest mechanical strength and carbon yield among all the other polymer precursors. Moreover, PAN has a higher electrospinning ability compared to the other polymers.[23] It is already well established that the preparation of CNFs from electrospun PAN nanofiber precursors involves two steps in different temperature ranges. The first one is the oxidative stabilization of PAN fibers in air between 200 and 350 °C. This step is essential to create a cyclic molecular structure through oxidation, dehydrogenization, and cyclization reactions. The second step is the carbonization of the stabilized PAN fibers between 600 and 1300 °C under N$_2$ or Ar flow, although the mostly employed temperature is 800 °C. During this last step, an aromatic honeycomb structure is formed due to the condensation of the stabilized PAN structure and the removal of nitrogen and oxygen atoms through formation of gaseous nitrogen oxides.[25,26] SCs devices based on CNFs are still characterized by relatively low values of C_s.[27–29] Indeed, there is a huge number of works discussing the possibility to tune the graphitization degree, to increase the surface area accompanied by controlled pore size distribution, and to increase the mechanical stability and we invite the interested reader to refer to ref. [23] to obtain a complete overview of the topic. However, the correlation between structure and physicochemical properties with capacitive behavior is only seldomly discussed and no systematic investigations have been carried out on understanding the effect of changing the thermal treatment parameters in order to tune C_s. In addition, the majority of the existing works is not examining in detail the electrochemical performance of pure CNFs, but always in combination with other active materials, in hybrid or composite structures, which does not allow to understand the actual role of the carbon species.[30–32] However, the optimization of PAN-based materials as CNFs templates for energy storage is extremely fruitful for the development of an emergent class of capacitors realized with block copolymers, in which the carbon matrix (such as PAN) is attached to a sacrificial block.[33,34] The research in this field is mainly focused on the stabilization of PAN at 300° and subsequent carbonization in nitrogen environment for forming the final porous carbon backbone,[35] thus maximizing the pseudocapacitive behavior by achieving the largest possible active area. It is thus important to better understand the potential of PAN-derived carbon nanomaterials in the field of energy storage, also given their versatility for combination with many other species, by fine-tuning the preparative process, in order to infer structure–property–function relationships.

With this work, we present an in-depth study on the optimization of CNFs production conditions from electrospun PAN and examine different stabilization (T_s) and carbonization (T_c) temperatures, in order to identify the best conditions for balancing N-doping, electrical conductivity, SSA, and pore size distribution, which are the main parameters influencing C_s in SC architectures.[36] We do this on the sole CNFs, and not on hybrid architectures with other active species, in order to understand their intrinsic electrochemical performance. This study is also motivated by the scarcity of investigations on this specific topic because the effect of the two thermal treatments on the indicated parameters is significant and these last ones are, in turn, determinant for driving capacitive behavior. The particular approach chosen here is to first compare different T_s while keeping fixed T_c, to characterize the influence of the former on the identified variables, and then to proceed with optimization of the latter. With this method, an ideal two-step temperature treatment to obtain the best capacitance from CNFs can be identified.

2. Results and Discussion

CNFs were prepared in three steps, by first electrospinning PAN to obtain polymeric nanofibers, followed by stabilization of the resulting fibrous scaffolds in air and by final carbonization under nitrogen. The stabilization and carbonization temperatures were varied within a range, in order to understand the effect of these thermal treatments on the physical and electrochemical properties of the resulting CNFs. **Figure 1** shows a schematic representation of the process, with details on operative conditions for each involved step.

A rational systematic variation of conditions was applied to prepare the different CNFs samples, by considering first the tuning of T_s while maintaining T_c at the classical 800 °C, which is the most common condition used in the literature for this second step. Then, within these samples, the T_s of the best performing one from the electrochemical point of view (vide infra) was kept fixed and a variation of ±100 °C was applied to the standard T_c, i.e., T_cs of 700, 800, 900 °C were investigated. This approach allows to understand in two separate steps the effect of stabilization and carbonization processes leading to optimized electrochemical performance of CNF-based electrode materials.

The electrochemical performances of symmetrical SC based on CNFs in 1 M of H$_2$SO$_4$ are reported in **Figure 2**. The GCD curves at 2 A g^{-1}, presented in Figure 2a, underline the linear relationship between the potential and the time which leads to a triangular charge/discharge curve which is characteristic of electric double-layer materials (experimental CV and GCD curves for all samples are shown in Figure S4 and S6, Supporting Information). In each GCD curve it is possible to identify the IR drop, which is associated with the internal resistance.[37] The CV curves at 50 mV s^{-1} (Figure S4, Supporting Information) show a characteristic rectangular shape of electric double-layer materials, in accordance with GCD measurements. However, although the CV curves have a symmetric and almost ideal rectangular shape, the presence of equivalent series resistance (ESR) and equivalent parallel resistance (EPR) lead to small deviations from the ideal shape.[38] In addition, a slightly asymmetric shape, most likely caused by the distribution of ions in the double layer
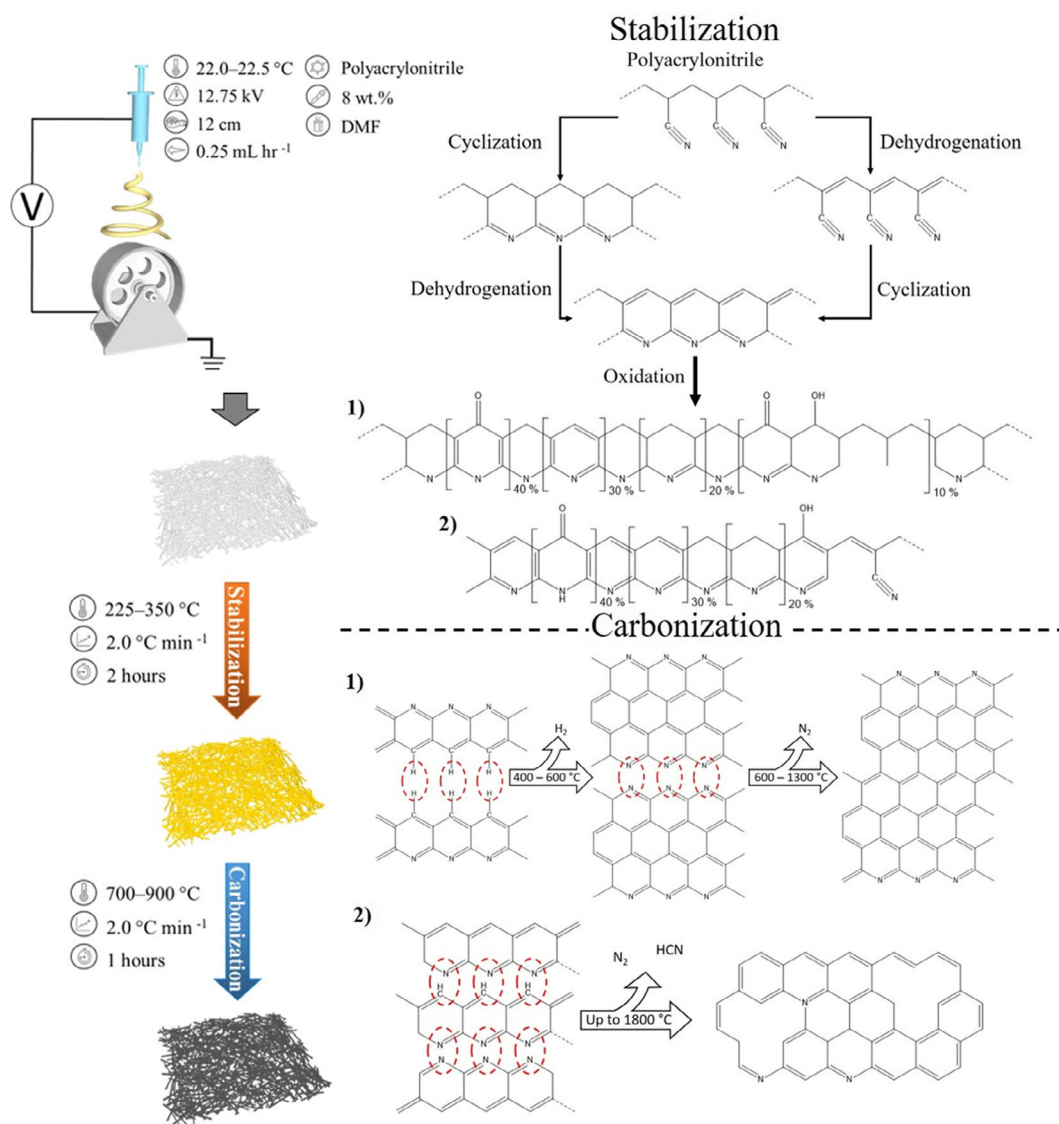
ADVANCED
SCIENCE NEWS
www.advancedsciencenews.com

ADVANCED
ENERGY & SUSTAINABILITY
RESEARCH
Open Access
www.advenergysustres.com

Figure 1. Schematic representation of the entire CNFs production process, including the electrospinning of PAN, stabilization, and carbonization steps parameters employed. The details on the chemical processes happening during the two steps are also shown for 1) defect-free[25] and 2) defect-rich phases.[82]

during the charge and discharge process, is observed. Especially at high scan rates, tail-like shapes are probably formed by redox processes (reactions) with the electrolyte or solvent. During the charging, fewer ions are in the proximity of the electrode surface, reducing the number of total charges detected by the external circuit. On the contrary, during the discharging, the electric double layer is larger due to the presence of more ions which increases the effective capacitance.[38] In the CVs, it is possible to identify some weak and broad peaks that can be associated with redox reactions due to the pseudocapacitance of nitrogen or impurities adsorbed on the surface.

A long discharge time in the GCD curves and a large area within the CV curves of the CNFs—325–800 sample implies a higher C_s than that of the all other samples examined. Indeed, as reported in Figure 2c,d, device based on CNFs—325–800

achieved the highest average value of C_s for all the current densities tested, except for 20 A g^{-1}. At 0.5 A g^{-1}, such sample shows an average C_S of 49 ± 3 F g^{-1}, which is reduced to 30 ± 3 F g^{-1} at 20.0 A g^{-1}. The same trend is seen in the Ragone plots presented in Figure 2e,f, where it achieves the highest average E_d of 4.4 ± 0.2 Wh kg^{-1} at a P_d of 200 W kg^{-1}. These values are further reported in **Table 1** and **2** for the sake of clarity. The promising electrochemical performance of CNFs—325–800 can be explained by a combination of different factors, as it will be clarified later in the text by analyzing XPS, physisorption, SEM, and EDX data.

EIS measurements were carried out to study the impedance behavior of the CNF-based devices and to confirm their capacitive properties. **Figure 3**a and S6, Supporting Information, represent the Nyquist plots of the SCs in the frequency range
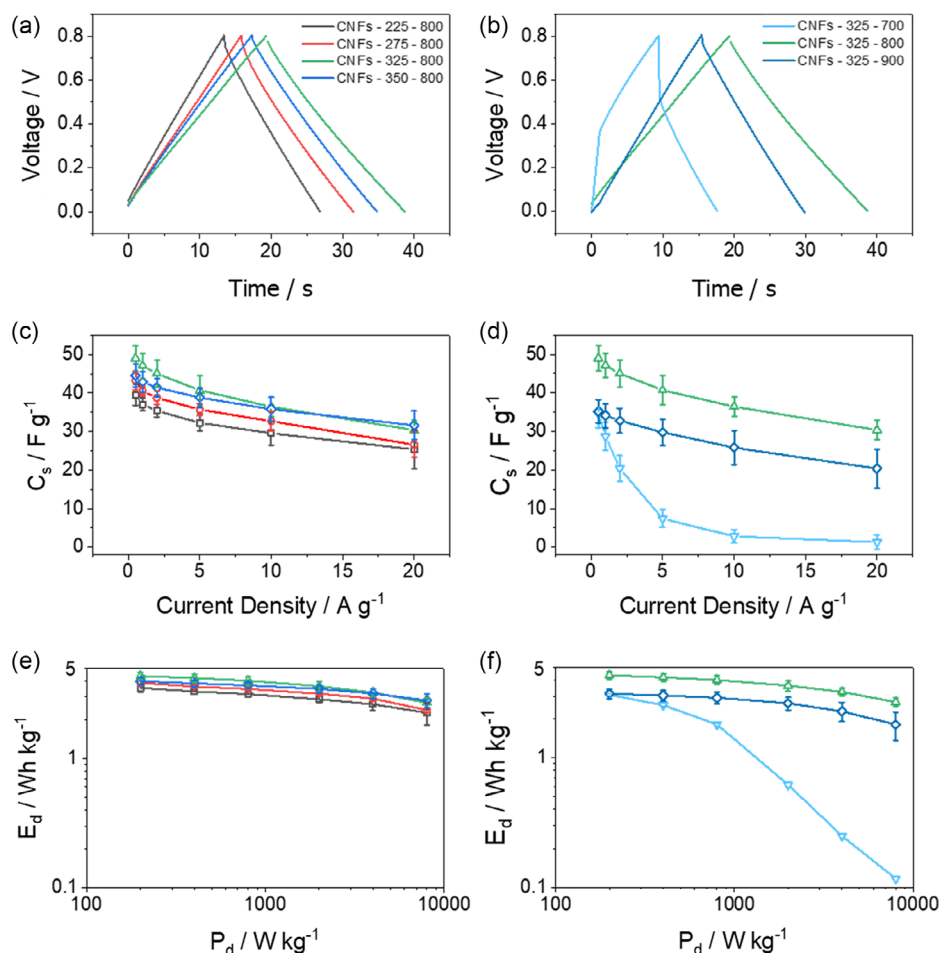
Figure 2. Comparison of the electrochemical performance of symmetric SCs based on the different CNFs used as electrode materials: a) GCD curves obtained at $2.0\,A\,g^{-1}$ in the 0–0.8 V range in 1 M H_2SO_4 electrolyte at different T_s; b) GCD curves obtained at $2.0\,A\,g^{-1}$ in the 0–0.8 V range in 1 M H_2SO_4 electrolyte at different T_c; c) trends in C_s as a function of current density for the different examined T_s; d) trends in C_s as a function of current density for different examined T_c; Ragone plots for e) different T_s and f) different T_c.

Table 1. Values obtained from the fittings of the EIS curves recorded for devices based on CNFs samples prepared at different T_s or T_c.

Device based on	R_s [Ω]	R_{ct} [Ω]	CPE_1 [10^{-5} S]	N_1	C_{dl} [μF]	CPE_2 [S]	N_2
CNFs—225–800	0.94	23.78	6.50	0.82	15.69	0.069	0.94
CNFs—275v800	0.85	14.60	5.20	0.83	17.78	0.084	0.96
CNFs—325–800	0.90	5.96	14.20	0.77	26.92	0.042	0.97
CNFs—350–800	1.00	14.50	15.10	0.77	21.83	0.052	0.93
CNFs—325–700	0.88	46.50	9.00	0.75	15.45	0.071	0.92
CNFs—325–900	0.90	1.70	13.00	0.81	18.04	0.062	0.92

between 200 kHz and 10 mHz. The Nyquist plot can be divided into three regions. In the first one, the high-frequency region, the intercept with the real axis (Z'_{Re}) is related to the internal resistance (R_s) induced by the resistance of the electrolyte. In the second one, the midfrequency, the semicircle is associated with surface properties, which are related to the charge-transfer resistance (R_{ct}) between the electrode and electrolyte or contact between the electrode and current collector. In the last one, the low-frequency region, the straight line is related to the electric double layer's impedance. However, for an ideal capacitor, this line is parallel to the imaginary axis ($-Z'_{Im}$). Instead, for a real capacitor, this line has a slope determined by the presence of resistances.[39,40] The experimental data were fitted with a modified Randles circuit to evaluate the values of R_s, R_{ct}, and double-layer capacitance (C_{dl}), as reported in the inset in Figure S6, Supporting Information and in Table 1.[41] Constant phase elements (CPEs) were chosen for modeling the Warburg element and C_{dl}. With CPEs, the nonideality of the device can be modeled with more accuracy and include the role of each element. CPE_1 is related to the C_{dl}, while CPE_2 is associated with the Warburg coefficient, determined by the semi-infinite diffusion of the ions in the electrolyte.[42,43] The C_{dl} was calculated using the equation reported by Bard and Faulkner.[44] From the fittings, all the samples exhibit slightly different values of R_s, within 10% error. Indeed, the impedance behavior of the devices is mainly determined by R_{ct}, which shows

Table 2. Comparison of electrochemical performances for the symmetric devices indicated in Figure 8. ΔV stands for the potential range used for the measurements. If it is indicated with a minus sign, it means that the devices were tested in a negative potential range.

| Type of sample	P_d [W kg^{-1}]	E_d [Wh kg^{-1}]	Electrolyte	$\Delta V/V$	Ref.
Flexible porous CNFs	600	3.2	0.5 M H$_2$SO$_4$	1.2	[71]
Activated CNFs	900	5.0	1.0 M Na$_2$SO$_4$	1.8	[72]
AC	1500	4.2	1 M H$_2$SO$_4$	1.0	[74]
CNTs with N-doped carbon	200	1.0	1 M H$_2$SO$_4$ (Swagelok cell)	0.8	[73]
B, N co-doped CNs	600	4.2	1 M H$_2$SO$_4$	0.8	[75]
Oxigenated N-doped CN	1200	3.4	6 M KOH	-1.0	[76]
N, F co-doped CNFs	248	8.7	1 M H$_2$SO$_4$ (Gel electrolyte)	1.0	[77]
Porous AC/graphene	8000	4.4	6 M KOH (Coin cell)	0.8	[78]
CNFs—325–800	800	4.0 ± 0.3	1 M H$_2$SO$_4$ (Swagelok cell)	0.8	This work
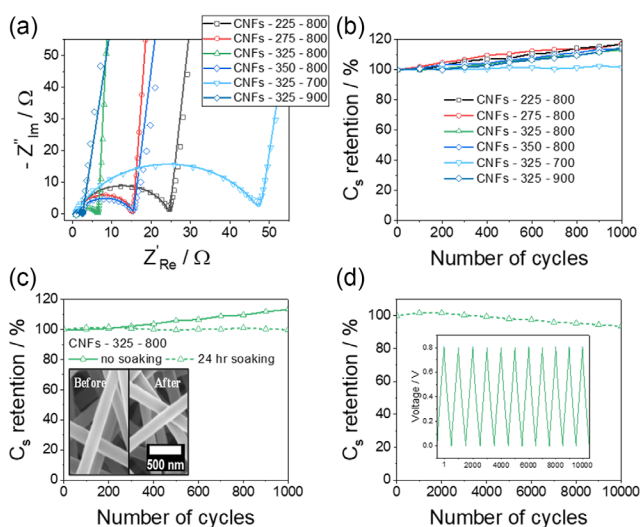
Figure 3. a,b) Nyquist plots obtained from EIS of CNFs samples prepared at different T_s or T_c. c) Capacitance retention of the devices based on CNFs—325–800 after 1000 cycles. The dashed blue line indicates the data associated to the device with the electrode materials soaked in the electrolyte solution for 24 h. The solid line refers instead to the data obtained when the electrode materials were not soaked before the preparation of the device. e) Capacitance retention of the devices based on CNFs—325–800 after 10 000 cycles. The electrode materials were previously soaked for 24 h in the electrolyte solution.

the most prominent difference between each sample. Indeed, an ideal double-layer capacitor does not exhibit a R_{ct} because there is no charge transfer but only electrostatic interactions between the electrodes and electrolyte. In addition, all the devices were closed by applying the same pressure. It is reasonable, therefore, that these values of R_{ct} are probably due to the presence of nitrogen, which introduces a pseudocapacitive behavior to the system. As it can be tracked from Table 1, the R_{ct} follows indeed the, later explained, same trend of nitrogen concentration in the samples (Table S2, Supporting Information). The straight line in the low-frequency region achieves the highest slope for the device based on CNFs—325–800, suggesting a better capacitive behavior. This is also confirmed by the calculation of the C_{dl}, which is the

highest for CNFs—325–800. In conclusion, EIS results further confirm that CNFs—325–800 has the best electrochemical properties as a SC, compared to the other samples.

Regarding the stability of the best SC device (i.e., the one based on the CNFs—325–800 sample), Figure 3c shows the capacitance retention tested at a current density of 2.0 A g^{-1} for 1000 cycles. All the examined samples achieved comparable and stable cycle performances, with capacitance retention between 113% and 117%. The increase in capacitance retention has already been reported for other carbon-based materials and it can be associated to a self-activation process and/or to the pore size distribution.[45–47] The self-activation process induces changes in the surface morphology, especially because it may increase the SSA. Also cycling the sample may cause changes in the equilibrium states of the sample. These states might be induced by the repeating charging/discharging, modifying the morphology, and further exposing the electrochemically active sites to the electrolyte.[48,49] In the inset in Figure 3c, SEM images of CNFs—325–800 before and after the stability test are reported. As far as it can be observed, the surface morphology has not changed after 1000 cycles. Regarding the pore size distribution, as the CNFs are characterized by micropores, the electrolytes take time to fill all the pores. As a result, at the beginning of the measurements, not all the surface is in touch with the electrolyte and contributes to the capacitance. To verify this assumption, the stability test for CNFs—325–800 was repeated but the electrode materials were previously immersed in the electrolyte solution for 24 h (Figure 3c, dashed green line). As it can be seen, the capacitance retention after the 1000 cycle does not increase but remains stable, also indicating a good cycle performance, which is confirmed after 10 000 cycles (94% of capacitance retention), reported in Figure 3d. The excellent capacitance retention can be explained by the large SSA of up to 220 m^2 g^{-1} and the existence of short pore channels. The small capacitance decrease can be attributed to changes in the defects structure during cycling.[50]

Figure 4a,b and S7a–e, Supporting Information, present the SEM images of carbonized PAN fibers. For each sample, the diameter is distributed uniformly, and the fibers do not show any particular defect (such as bead defects), underlying that the electrospinning deposition process was optimized. T_c appears to be the key parameter defining the final CNF diameter,
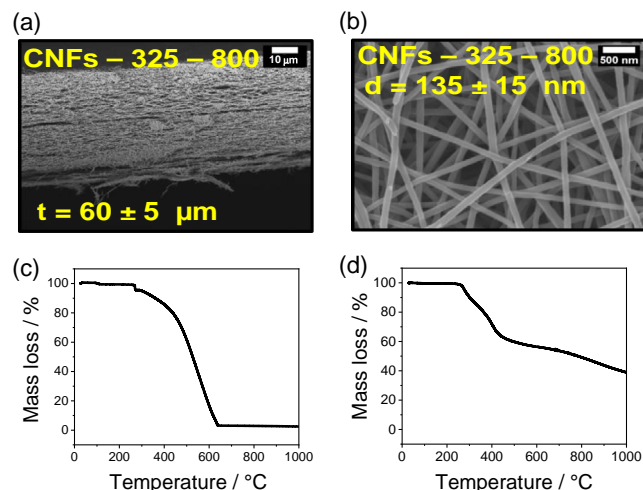
Figure 4. a) Cross-sectional SEM image of the CNF—325–800 sample. The thickness (t) is reported. b) Top-view SEM image of the same sample. c) TGA analysis of electrospun PAN fibers heated up to 1000 °C in synthetic air (stabilization conditions). d) TGA analysis of stabilized PAN fibers heated up to 1000 °C under nitrogen atmosphere (carbonization conditions).

Figure 5. a–c) Nitrogen physisorption isotherms and b–d) relative pore size distribution curves for CNFs samples prepared at different T_s or T_c (the graph is a zoom at the lowest pore sizes of the inset, reporting the entire distribution up to 30 nm).

while T_s is not affecting the thickness. This can be explained by the mass loss during the stabilization and carbonization processes, which can be determined by TGA analysis, as reported in Figure 4c,d. During stabilization (225–350 °C, Figure 4c) the mass loss is around ≈6 wt%. On the other hand, during carbonization, (700–900 °C, Figure 4d) the mass loss is increasing up to ≈13 wt%. Indeed, the value slowly approaches a plateau (within the error bar) when the stabilization temperature is increased. When T_c is increased from 700 up to 900 °C instead, the diameter decreases significantly (Figure S7, Supporting Information). Finally, the thickness of the deposited fiber mats can be determined from cross-sectional SEM analysis to be in the 60 μm range for all samples. Figure 4a shows a prototypical image, referring to the sample treated at 325 and 800 °C for, respectively, T_s and T_c.

Nitrogen physisorption was performed to evaluate specific information regarding fibers' morphology, namely, SSA and pore size distribution. For the applications of CNFs as electrode material for SC devices, a large electrode–electrolyte interfacial contact is indeed essential to enhance the charge transfer and the charge adsorbed. However, a high SSA is useless if the pore size distribution is not optimized because this last one may limit the accessible surface to the electrolyte. In **Figure 5**a–d, the isotherms and pore size distributions are reported. As it can be deduced from the reported values in the graphs, SSAs vary mostly in relation to changes in T_c, with variations of 100–220 m^2 g^{-1} when this temperature is raised by 100 °C (see Figure 5c). Pore sizes are also quite homogeneous in relation to different T_s and same T_c, while they tend to change slightly more when T_s is taken stable and T_c is varied. In general, their distribution is centered around 1 nm, with a population more shifted at higher values (up to 2 nm) for the sample treated at the highest T_c (900 °C).
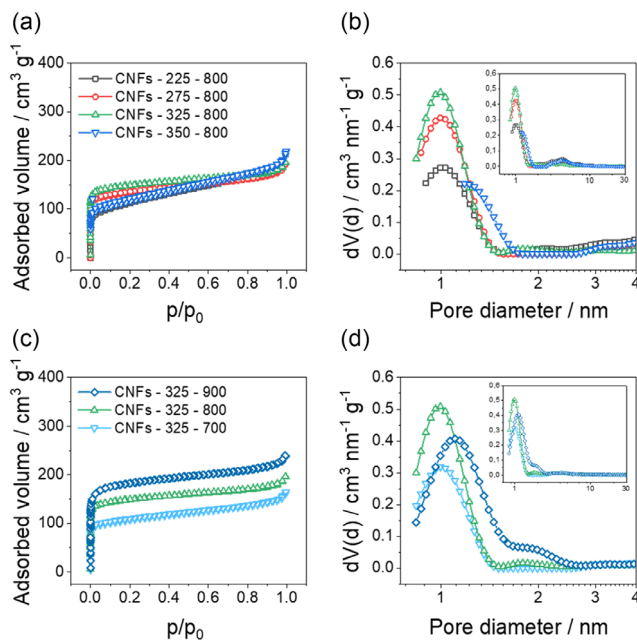
XPS measurements were performed to understand how nitrogen heteroatoms, acting as N-dopants, are inserted into the main graphitic structure of the CNFs. This evaluation is extremely important to better understand the structural and electrochemical performance of CNFs. As displayed in **Figure 6**a, CNFs exhibit four main types of nitrogen bonding, namely, pyridinic (N-6, at 398.1–398.3 eV), pyrrolic (N-5, 399.8–401.2 eV), graphitic (N-Q, 401.1–402.7 eV), and oxidized (N-O, 403–406 eV).[51,52] Therefore, the chosen energy range for XPS analysis was between 200 and 600 eV to detect the O 1s, N 1s, and C 1s signals (see the whole spectrum in Figure 6b for one prototypical case and all the others in Figure S8, Supporting Information). The signal of C 1s localized at 284.8 eV mainly shows the sp^2-hybridization (graphitic) of the carbon atoms in the CNFs, whereas the peak asymmetry toward higher binding energies can be ascribed to the presence of defects based on sp^3-hybridized carbon species like C–C (284.7 eV) or C–OH (285.4 eV) present within the CNF lattice.[53,54]

In the region of the N 1s peak between 394 and 408 eV, more detailed spectra were recorded, to precisely analyze the above-described multiple nitrogen species and to define their contribution to the nitrogen peak in each spectrum (see also Table S2, Supporting Information). In order to first understand the influence of different T_s in the range 225–350 °C (Figure 6c and S9, Supporting Information), XPS data as well as EDX atomic percentages (at%) were employed for the evaluation (Table S2, Supporting Information). A trend in progressive nitrogen removal from the fibrous structure is observed from 225 °C (with ≈7.2–7.3%) up to 325 °C (with 5.1–6.0%), while stabilization at 350 °C brings to an increase for both elemental analysis methods between 6.0% and 6.8%, which is, to the best of our
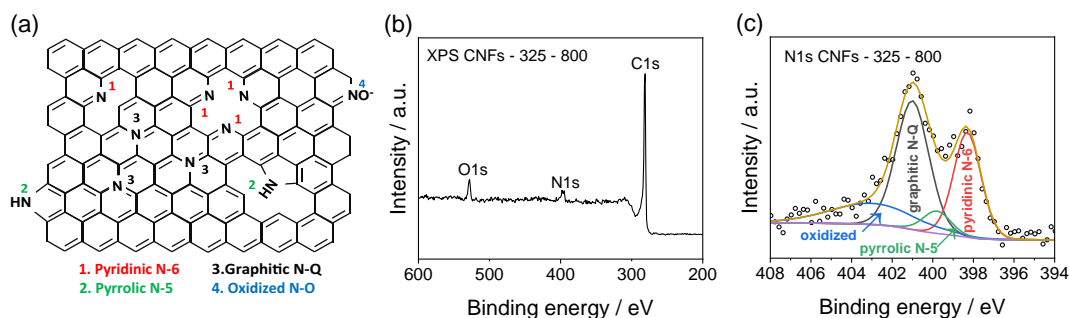
Figure 6. a) Schematic representation of different nitrogen species present in the CNF structure. b) Full XPS spectrum for CNFs—325–800 sample (the entire spectra for all other examined cases are reported in Figure S3, Supporting Information). c) Detail of the N 1s peak for the same sample, with fittings of the different nitrogen contributions.

knowledge, here reported for the first time. The two fundamentally different techniques here used also allow to assume a homogenous distribution of the doping along the whole CNF diameter. While XPS is surface sensitive and a local technique, the penetration depth of EDX (depending on the acceleration potential) can go up to several hundreds of nm, plus a broader investigated area. Therefore, depending on the stabilization temperature, a constant atomic ratio of nitrogen can be found throughout the CNFs as well as on their surface. Previously obtained data on nitrogen contents for CNFs stabilized at 225 °C and carbonized at 800 °C were fully reproducible in our work.[55] Increase in T_s leads to larger contributions of graphitic nitrogen, as can be guessed from XPS spectra, from 40% at 225 °C to 45% at 350 °C. On the contrary, the contribution of pyrrolic and pyridinic nitrogen atoms decreases from 10% to 6% for the former and from 35% to 28% for the latter. The oxidized species tend also to increase from 15% to 21%. This is reasonable given the more efficient oxidation (as well as partially graphitization) at higher temperatures during stabilization. In the case of the stabilized sample at 350 °C, another peak is further visible, attributed to $NO_2/C–ONO$ and NO_2^- nitrogen species, which can be formed at higher temperatures in the presence of oxygen and nitrogen.[56–58]

T_c is drastically affecting the amount of graphitic carbon within the CNFs. From 700 to 900 °C at a constant T_s (325 °C), an increase from 24% at 700 °C to 53% at 900 °C

was detected. As a consequence, the pyrrolic and pyridinic species contributions diminish from 22% down to 5% (N-5) and from 38% to 17% (N-6). These changes in composition are well described in literature, with the less stable pyrrolic nitrogen converting into graphitic nitrogen above 600 °C, while pyridinic nitrogen converting in the same species above 700 °C.[55,59,60] This is indeed confirmed by our experiments, where N-5 content decreases already drastically from 700 to 800 °C (22% to 7%), while N-6 content experiences a drop from 38% to 17% over the whole examined T_c range (700–900 °C).

Raman and XRD analyses were carried out to study changes in the graphitic microstructure of the CNFs and to determine the influence of nitrogen concentration and types of nitrogen. The Raman spectrum of the electrochemically best performing CNF sample is presented in **Figure 7**a, while the list of parameters calculated from Raman spectroscopy for all the samples is reported in Table S3, Supporting Information. For comparison, the other Raman spectra are shown in Figure S10, Supporting Information. Peaks deconvolution shows that all samples have four contributions. Peaks at ≈1590 and ≈1350 cm^{-1} are associated with the G and D bands, related to ordered and disordered graphitic structures, respectively.[61,62] The D″ band at ≈1500 cm^{-1} is related to the amorphous carbon and the I band at ≈1220 cm^{-1} is associated with the bond between sp^2 and sp^3 carbons.[63–65] One of the most important parameters for carbon materials is the I_D/I_G ratio. As G bands correspond to the E_{2g}
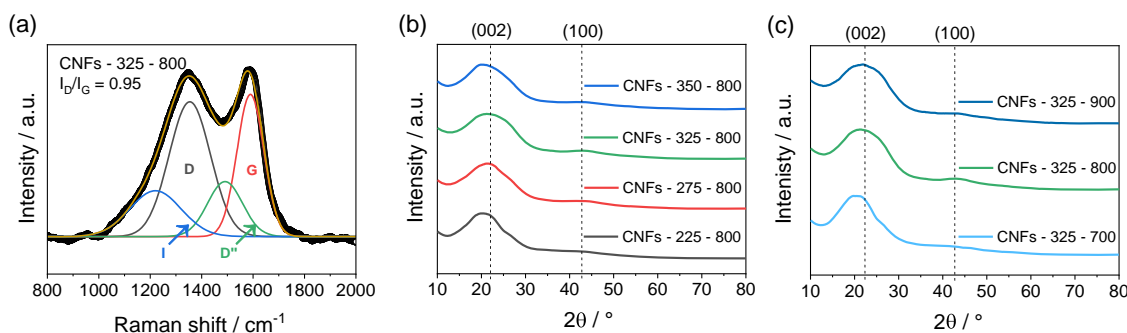

Figure 7. a) Raman spectrum of the CNF—325—800 sample. b) XRD patterns of CNFs samples prepared with varying T_s from 225 °C up to 350 °C and a constant T_c at 800 °C. c) XRD patterns of CNFs stabilized at 325 °C with varying T_c from 700 °C up to 900 °C. These structures correspond to JCPDS 00-056-0159.

**ADVANCED
SCIENCE NEWS**

www.advancedsciencenews.com

**ADVANCED
ENERGY & SUSTAINABILITY
RESEARCH**
Open Access

www.advenergysustres.com

phonon which is always present, the D band, on the contrary, is related to the breathing mode and therefore requires defects to be activated. Indeed, the more defects are present in the graphitic structure the higher the I_D/I_G ratio will be.[61,62] Defects are not only atomic vacancies or distortion of the structure but also defined by the presence of heteroatoms (see Figure 6a). As already reported, the amount of carbon defects in nitrogen-doped carbon materials is strongly depending on nitrogen amount and relative bonds involved.[66] From XPS and EDX measurements emerges how the overall nitrogen amount decreases with higher T_s and T_c and, at the same time, graphitic carbon content increases. This also affects the order of CNF microstructure. Indeed, I_D/I_G ratio (Table S3, Supporting Information) shows the same trend of graphitic nitrogen contribution (Table S2, Supporting Information): it generally decreases at larger T_s and T_c. The rising G band in comparison to the D band is indicating a more structured carbon lattice at higher temperatures.[61,62] From the collected dataset however, deriving a clear trend in either changes of amorphous carbon content (D″ band) or sp^2–sp^3 bonds (I band) is not possible in a reliable manner.

A further proof of the influence of nitrogen concentration on CNFs microstructure can be determined by XRD measurements. Figure 7b,c and Table S4, Supporting Information, show the XRD data and a list of parameters calculated from the diffractograms, respectively. Those diffractograms are characterized by a major Bragg peak at 21.0° and a weak reflex at 43.0°, which are related to crystal planes (002) and intralayer scattering (100) of graphite.[67,68] An important parameter for materials with a graphite-like structures is the interlayer distance along the (002) direction: $d_{(002)}$. This parameter is essential because the presence of nitrogen atoms, and consequently a more disordered graphitic structure, leads to higher values of $d_{(002)}$ compared to that of graphite 3.335 Å.[55,67–69] Indeed, the values of $d_{(002)}$ (Table S4, Supporting Information) are higher than 3.335 Å due to the presence of nitrogen atoms. Moreover, $d_{(002)}$ show the same trend of the nitrogen concentration reported in Table S2, Supporting Information: it decreases with the increasing of stabilization and carbonization temperatures.

Other important parameters that can be evaluated from Raman spectroscopy and XRD measurements are related to the crystallite size: in-plane crystallite size L_a along a-direction and average stacking height L_c along the c-direction. Through this analysis, preferential growth directions of the microstructure can be determined. Values of L_a, reported in Table S3, Supporting Information, can be easily determined from Raman spectra by using the Tuinstra–Koening equation, while values of L_c, presented in Table S4, Supporting Information, can be estimated from XRD diffractograms by applying the Scherrer equation. As reported, graphitic structure grows along L_a with the rising temperatures; on the contrary, L_c decreases. The decrease along c-direction can be explained by two possible phenomena: 1) changes in stacking and order for graphitic structure along due to the release of gases during the thermal treatments[55] and 2) curvature of the graphene sheets due to the presence of nitrogen doping heteroatoms.[70]

To summarize, the low concentration of nitrogen, especially with a high contribution of graphitic nitrogen, leads to a more ordered graphitic structure (low $d_{(002)}$ and I_D/I_G). Moreover,

CNFs structure grows mainly along in-plane a-direction, as evidenced by the increase of L_a. On the other hand, the growth of graphite sheets along the c-direction is disturbed and reduced.

The results as a whole give a fully satisfactory picture of the CNFs functional behavior, allowing to provide a speculative, but pragmatic, correlation between electrochemical performance and morphological/structural properties. By examining the reported effects on stabilization derived from physisorption and XPS measurements, it is possible to understand electrochemical data more precisely. Indeed, the CNFs—325–800 sample, which is the most performing one, has also the highest SSA compared to other samples treated at different T_s. Regarding the effect of T_c, the electrochemical performances of CNFs—325–800 is a consequence of the balance between the SSA, total amount of nitrogen, and the contribution of each nitrogen bond-type. CNFs—325–700 has the highest amount of nitrogen, the lowest contribution of graphitic nitrogen, and lowest value of SSA, leading to a lower average value of C_s. On the contrary, even if CNFs—325–900 shows the highest SSA, it does not achieve the average value of C_s of CNFs—325–800, due to the lower nitrogen concentration, leading to a too low defect density. Indeed, this result is further corroborated by Raman analysis, in which the lattice defects density, in terms of graphitic nitrogen contribution, is diminished at higher T_s and T_c. In addition, the lattice parameters are also strongly influenced by the nitrogen doping as highlighted by the XRD outcomes: the best electrochemical samples are the ones in which the interlayer distance $d_{(002)}$ is among the smallest (4.1 Å), with an anisotropic growth on the in-plane a-direction.

In the literature, numerous works on the preparation and application of carbon-based materials in energy storage devices are reported. **Figure 8** compares the performance of the devices tested in this work with different similar symmetrical SCs. The best obtained values of E_d and P_d from the here studied CNFs are compared with that of other relevant cases of carbon-based materials, such as flexible porous CNFs (3.2 Wh kg^{-1} at a P_d of 600 W kg^{-1}),[71] activated CNFs (5.0 Wh kg^{-1} at a P_d of 900 W kg^{-1}),[72] CNTs with N-doped carbon (1.0 Wh kg^{-1} at a P_d of 200 W kg^{-1}),[73] AC (4.2 Wh kg^{-1} at a P_d of 1500 W kg^{-1}),[74] B, N co-doped CN (4.2 Wh kg^{-1} at a P_d of 600 W kg^{-1}),[75] and oxygenated N-doped CN (3.4 Wh kg^{-1} at a P_d of 1200 W kg^{-1}).[76] Obviously, there are examples of carbon-based materials with more promising performance.
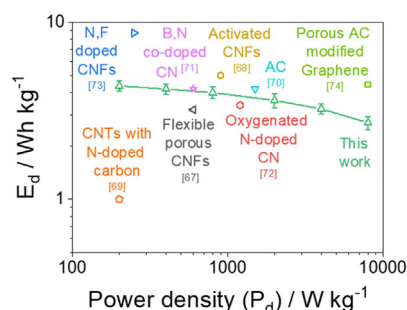

Figure 8. Ragone plot for the symmetrical device based on CNFs—325–800 compared with other symmetrical devices based on different carbon-based active electrode materials.

For example, Na et al. have successfully prepared highly porous N, F co-doped CNFs achieving an E_d of 8.7 Wh kg^{-1} at a P_d of 248 W kg^{-1}, but they used a vacuum plasma treatment with C_4F_8 after the carbonization step.[77] Chen et al. produced porous graphitic layers on both sides of graphene sheets through hydrothermal and activations steps, achieving an E_d of 4.4 Wh kg^{-1} at 8000 W kg^{-1}.[78] However, it is important to underline that CNFs produced in this work are made without any further processes such as activation or chemical etching and without any further additive. They indeed achieve these significant E_d value only by optimizing the heat treatment temperatures. In addition, as reported in Table 2, the devices tested in this work have been cycled in a potential range of 0.0–0.8 V ($\Delta V = 0.8$ V). As E_d is proportional to ΔV (Equation (6)), by increasing the latter E_d increases significantly. For a more complete comparison, Equation (S4), Supporting Informationm was used to estimate C_s of the single electrode. In Table S7, Supporting Information, the values of C_s for other CNFs are compared to the ones of the CNFs tested in this work. CNFs produced in this work are made without any specific processes of activation and chemical etching and without any further additives such as PVP or Co_3O_4. Indeed, as can be seen from Table S7, Supporting Information, the calculated C_s of CNFs prepared in this work is comparable with that one of other studies.

3. Conclusions

A systematic study to reveal the effect of different T_s and T_c on CNFs electrochemical performance was carried out in this work, by correlating their structural and compositional changes to C_s of symmetrical SC devices based on these pure materials as the only active electrode components. The different thermal treatments affect the SSA of the fibers, the amount of nitrogen atoms within their crystalline lattices, and the type of bonding that these heteroatomic dopants establish with carbon. The last two features also influence the microstructure of the CNFs and all together have a tremendous impact on the electrochemical behavior. As a rule of thumb, one can recognize that, with increasing temperatures, the SSA and the amount of graphitic (N–Q) nitrogen in the lattice increase, which lead to larger C_s and thus better energy storage performance.

A T_s of 325 °C for the produced PAN fibers was found to be ideal because the attainable SSA is the largest. Furthermore, these fibers contain the lowest nitrogen concentration, including the largest ratio of graphitic nitrogen compared to all the other samples produced at T_s of 225, 275, and 350 °C. Below the ideal temperature, the larger nitrogen content, as well as their bonding type (lowest ratio of graphitic nitrogen), leading to a more unorganized carbon structure, and the lower SSA give rise to poorer electrochemical performances. On the other hand, stabilization at 350 °C might cause pore blocking, that is negatively affecting the SSA and deteriorates electrochemical performance, due to a lower effective area and a less accessible surface.

The ideal T_c for the stabilized fibers was found to be 800 °C, once again because of optimal SSA, nitrogen concentration, and nitrogen bonding types. Higher temperatures are thus not necessary to improve electrochemical quality. Even if the high nitrogen concentration generates several defects for possible charge

storage processes, the comparably lower SSA at 700 °C causes a less accessible surface for the electrolyte–CNFs interaction, which worsen the electrochemical performance. On the other hand, the sample carbonized at 900 °C has the largest SSA and, therefore, the largest accessible area for the electrode–electrolyte interaction, but nitrogen content is the lowest in all the examined samples. In conclusion, there is a net trade-off between a large pseudocapacitive contribution of pyrrolic and pyridinic nitrogen species in the CNFs and a low SSA or vice versa, to be taken into consideration to achieve optimized energy storage performance. This aspect will most likely have an impact also for the use of CNFs in other electrochemical devices, such as batteries or sensors, and therefore the optimization here described will have a broader impact for the electrochemical community.

One key factor for optimized electrode materials based on carbon is to find the ideal temperatures for stabilization and carbonization, to maximize the defects contributing to the pseudocapacitive behavior and to achieve the largest possible accessible area, which is one of the big advantages of using similar materials for electrochemical applications. Then, even without further doping, complex processing and treatments and coupling with other materials, it is possible to produce competitive carbon-based active electrodes for SCs by only tuning thermal treatments, thus improving the sustainability of the production process.

4. Experimental Section

All chemicals and solvents were purchased from Sigma–Aldrich and used as received, unless otherwise specified. Milli-Q water was used as solvent for the preparation of the electrolytes for the electrochemical measurements.

CNFs Production: For the preparation of CNFs, a solution of 8 wt% of PAN (>99.0%, M_w 150 000) in DMF was prepared by dissolving 1.131 × g of PAN in 15 mL of DMF. A home-made electrospinning setup was employed (Figure S1, Supporting Information), made of two high voltage power supplies (Scientific Instruments, TSI-HV), a syringe pump (HARVARD APPARATUS, PHD 2000 Infusion), a syringe, a needle (inner diameter 1.2 mm, 18 G), and an aluminum foil-covered rotating drum collector (radius of 5 cm). The deposition parameters were chosen by following the work of Einert et al.[55] The tip-to-collector distance was fixed at 12 cm and the rotation speed of the drum at 65 rpm. The flow rate was set to 0.25 mL h^{-1} and a voltage of 12.75 kV was applied between the tip and the collector (+10.75 kV at the needle and −2.00 kV at the collector). As the electrospinning setup is placed in a closed box, the relative humidity is controlled and was set between RH = 30% and 35% at a temperature of 21 °C. The precursor PAN fiber mats appeared as reported in Figure S1b,c, Supporting Information. After the electrospinning deposition, the fibers were stabilized at 225, 275, 325, or 350 °C for 2 h, with a heat rate of 2 °C min^{-1} in air in a Nabertherm N7/H-P320 oven. Afterward, the stabilized fibers were carbonized under nitrogen flow at 100 °C for 1 h followed by a temperature increase up to 700, 800, or 900 °C for 1 h using a tube furnace (Nabertherm R80/300/11-P300). The nitrogen flow was fixed at 100 mL min^{-1} (100 sccm) and the heating rate at 2 °C min^{-1}.

CNFs Electrochemical Characterization and SC Assembly: To classify the produced samples based on their electrochemical performances, all electrochemical measurements were carried out in a two electrode Swagelok cell setup, as sketched in Figure S2, Supporting Information. The electrolyte was a 1 M aqueous solution of H_2SO_4 (1 mL). A glass microfiber separator without binder purchased by ALBET LabScience (GF 50 150) was used between the two half cells to prevent short-circuiting.

The electrochemical analyses were performed using the potentiostat and galvanostat Autolab (Metrohm). The software used to collect the data was Nova 2.1 (Metrohm). Electrochemical impedance spectroscopy (EIS) measurements were carried out with a SP 200 potentiostat from BioLogic. The software used to collect EIS data was EC-lab. Cyclic voltammetry (CV) measurements were carried out to verify the electric double-layer behavior of CNFs. In particular, the measurements were performed between 0 and 0.8 V at different scan rates of 100, 50, 30, 20, and 10 mV s^{-1}. Moreover, each cycle was performed four times and only the last one was used for data analysis to ensure reproducible voltammograms in equilibrium. Galvanostatic charge–discharge (GCD) measurements were performed to determine the capacitance retention of the Swagelok cell setup as well as the power and energy densities of the SCs. First, devices were cycled ten times between 0 and 0.8 V at 1.0 A g^{-1}. Then, charge and discharge curves were measured between 0 and 0.8 V at different current densities of 0.5, 1.0, 2.0, 5.0, 10.0, and 20.0 A g^{-1}. The specific capacitance was calculated with the following equation

$$C_s = \frac{I \Delta t}{m \Delta V} = [\text{F g}^{-1}] \tag{1}$$

where I is the charge–discharge current, Δt the discharge time, m the total mass of the electrodes ($\approx$15.0 mg), and ΔV the potential range of the measurements (0.8 V). Each measurement, at the same current density, was performed three times and only the last one was used for data analysis. E_d and P_d can be calculated directly from the results obtained from the charge and discharge curves. E_d and P_d were calculated by the following equations

$$E_d = \frac{1}{2} C_s \Delta V^2 \frac{1}{3.6} = [\text{Wh kg}^{-1}] \tag{2}$$

$$P_d = \frac{E_d}{\Delta t} 3600 = [\text{W kg}^{-1}] \tag{3}$$

The values reported for C_s, E_d, and P_d are average values calculated by repeating the measurements with at least three different devices for each sample. To study the life cycle stability of the device, capacitance retention was calculated by cycling the device for 1000 and 10 000 cycles at a moderate current density of 2.0 A g^{-1}. EIS measurements were carried at a constant potential mode of 0 V. Frequency range was varied between 200 kHz and 10 mHz at an amplitude of 5 mV. Before each EIS measurement, five GCD curves were recorded at 1.0 A g^{-1} to stabilize the devices. The software to fit the obtained EIS data was RelaxIS3.

CNFs Physicochemical and Morphological Characterization: Raman spectroscopy measurements were performed on a Bruker Senterra Raman Microscope equipped with a 532 nm solid-state laser. As the fibers are free-standing, to obtain more detailed spectra, samples were attached to a silicon wafer (1 cm × 1 cm) with double tape. The in-plane crystallite dimension (L_a) can be calculated using the Tuinstra–Koening equation[79]

$$L_a = (2.4 \times 10^{-10}) \lambda^4 \left(\frac{I_D}{I_G} \right)^{-1} = [\text{nm}] \tag{4}$$

where λ is the wavelength of the laser in nm, and I_D/I_G is the intensity ratio between the D and G bands.

X-Ray diffraction (XRD) measurements were carried out on a PANanalytical X'Pert PRO MRD (Cu Kα radiation, $\lambda = 1.5406$ Å) utilizing a grazing incident geometry (GIXRD). The diffractograms were recorded between $2\theta = 10°$ and 80° with an emission current of 40 mA and an acceleration voltage of 40 kV. The step size and the acquisition time were fixed at 0.03° and 2 s, respectively. The interlayer distance $d_{(hkl)}$ between the crystallographic plane (hkl) can be estimated by using the well know Bragg's law[80]

$$n\lambda = 2d_{(hkl)} \sin \theta \tag{5}$$

where n is the diffraction, λ is the wavelength of X-Ray in Å, and θ is the Bragg angle in radiant. If the diffraction order is 1, the Equation (2) can be written as follows

$$d_{(hkl)} = \frac{\lambda}{2 \sin \theta} = [\text{Å}] \tag{6}$$

The crystallite size (L_c) can be calculated using the Scherrer equation[81]

$$L_c = \frac{K\lambda}{\text{FWHM} \cos \theta} = [\text{Å}] \tag{7}$$

where K is a constant called shape factor ($\approx$0.9 for spherical particles), λ is the wavelength of X-Ray in Å, FWHM is the full width at the half maximum of the reflection, and θ is the Bragg angle. FWHM and θ must be radiant.

Thermogravimetric analysis (TGA) was run on a Netzsch STA409PC instrument. $\approx$10 mg of vacuum-dried PAN fibers were heated between 30 and 1200 °C with a ramp of 2 °C min^{-1} in nitrogen and synthetic air atmosphere.

Nitrogen physisorption was carried out in an automated gas adsorption station at 77 K with a Quantachrome Corporation Autosorb iQ2. Before each measurement, the sample was degassed at 120 °C for 18 h. The instrument's software supports the calculation of SSA by applying the Brunauer–Emmett–Teller (BET) model and pore size distribution, cumulative surface area, and pore volume with the quenched solid density functional theory (QSDFT, "cylindric pores, QSDFT adsorption branch").

X-Ray photoelectron spectroscopy (XPS) measurements were conducted with a PHI 5000 VersaProbe II Scanning ESCA Microprobe (Physical Electronics) with a monochromatized Al Kα X-Ray source in high power mode (beam size 1300 μm × 100 μm, X-Ray power: 100 W). The sample surface was charge neutralized with slow electrons and argon ions, and the pressure was in the range of 10^{-7} to 10^{-6} Pa during the measurements. The electron energy analyzer was working at a constant pass energy of 187.85 and 23.50 eV for survey and detail spectra, respectively. Data analysis was performed using the CasaXPS software. The C 1s line at 284.8 eV was used as binding standard energy to correct the position of the spectra. The Shirley-type function was used for background subtraction. The N 1s peaks were fitted by a mixed Gaussian/Lorentzian function (GL30).

The morphology of CNFs was investigated by scanning electron microscopy (SEM) on a Zeiss Merlin with an emission current of 100 pA and an acceleration voltage of 3 kV. The PAN and PAN-stabilized fibers, which are insulating, were sputtered with platinum for 60 s prior to each SEM measurement, using an Edwards scancoat six. The atomic concentration of carbon, nitrogen, and oxygen was determined by energy-dispersive X-Ray (EDX) analysis using an Oxford Instrument Inca Energy System X-Max 50 Silicon Drift Detector with a 50 mm^2 active area, an emission current of 2000 pA and an acceleration voltage of 5 kV. To obtain a more precise atomic concentration, EDX measurements were performed six times for each sample to calculate an average value.

Supporting Information

Supporting Information is available from the Wiley Online Library or from the author.

Acknowledgements

Conflict of Interest

The authors declare no conflict of interest.

2300121 (10 of 12)

Data Availability Statement

The data that support the findings of this study are available from the corresponding author upon reasonable request.

Keywords

[1] A. Ometov, V. Shubina, L. Klus, J. Skibińska, S. Saafi, P. Pascacio, L. Flueratoru, D. Q. Gaibor, N. Chukhno, O. Chukhno, A. Ali, A. Channa, E. Svertoka, W. Bin Qaim, R. Casanova-Marqués, S. Holcer, J. Torres-Sospedra, S. Casteleyn, G. Ruggeri, G. Araniti, R. Burget, J. Hosek, E. S. Lohan, *Comput. Networks* **2021**, *193*, 108074.

[2] R. T. Yadlapalli, R. Alla, R. Kandipati, A. Kotapati, *J. Energy Storage* **2022**, *49*, 104194.

[3] S. Cao, Y. Li, Y. Tang, Y. Sun, W. Li, X. Guo, F. Yang, G. Zhang, H. Zhou, Z. Liu, Q. Li, M. Shakouri, H. Pang, *Adv. Mater.* **2023**, *35*, https://doi.org/10.1002/adma.202301011.

[4] S. Zheng, Q. Li, H. Xue, H. Pang, Q. Xu, *Natl. Sci. Rev.* **2020**, *7*, 305.

[5] Y. Bai, C. Liu, T. Chen, W. Li, S. Zheng, Y. Pi, Y. Luo, H. Pang, *Angew. Chemie* **2021**, *133*, 25522.

[6] Poonam, K. Sharma, A. Arora, S. K. Tripathi, *J. Energy Storage* **2019**, *21*, 801.

[7] O. Barbieri, M. Hahn, A. Herzog, R. Kötz, *Carbon* **2005**, *43*, 1303.

[8] J. Gamby, P. L. Taberna, P. Simon, J. F. Fauvarque, M. Chesneau, *J. Power Sources* **2001**, *101*, 109.

[9] X. Li, C. Han, X. Chen, C. Shi, *Microporous Mesoporous Mater.* **2010**, *131*, 303.

[10] L. Z. Fan, Y. S. Hu, J. Maier, P. Adelhelm, B. Smarsly, M. Antonietti, *Adv. Funct. Mater.* **2007**, *17*, 3083.

[11] Y. Wang, Z. Shi, Y. Huang, Y. Ma, C. Wang, M. Chen, Y. Chen, *J. Phys. Chem. C* **2009**, *113*, 13103.

[12] X. Cao, Y. Shi, W. Shi, G. Lu, X. Huang, Q. Yan, Q. Zhang, H. Zhang, *Small* **2011**, *7*, 3163.

[13] H. Pan, J. Li, Y. P. Feng, *Nanoscale Res. Lett.* **2010**, *5*, 654.

[14] P. L. Taberna, G. Chevallier, P. Simon, D. Plée, T. Aubert, *Mater. Res. Bull.* **2006**, *41*, 478.

[15] C. Emmenegger, P. Mauron, P. Sudan, P. Wenger, V. Hermann, R. Gallay, A. Züttel, *J. Power Sources* **2003**, *124*, 321.

[16] C. Niu, E. K. Sichel, R. Hoch, D. Moy, H. Tennent, *Appl. Phys. Lett.* **1997**, *70*, 1480.

[17] R. Saliger, U. Fischer, C. Herta, J. Fricke, *J. Non. Cryst. Solids* **1998**, *225*, 81.

[18] P. Hao, Z. Zhao, J. Tian, H. Li, Y. Sang, G. Yu, H. Cai, H. Liu, C. P. Wong, A. Umar, *Nanoscale* **2014**, *6*, 12120.

[19] J. Li, X. Wang, Q. Huang, S. Gamboa, P. J. Sebastian, *J. Power Sources* **2006**, *158*, 784.

[20] C. Merino, P. Soto, E. Vilaplana-Ortego, J. M. De Gomez Salazar, F. Pico, J. M. Rojo, *Carbon* **2005**, *43*, 551.

[21] Z. Peng, J. Lin, R. Ye, E. L. G. Samuel, J. M. Tour, *ACS Appl. Mater. Interfaces* **2015**, *7*, 3414.

[22] A. Lamberti, F. Perrucci, M. Caprioli, M. Serrapede, M. Fontana, S. Bianco, S. Ferrero, E. Tresso, *Nanotechnology* **2017**, *28*, 174002.

[23] G. Nie, X. Zhao, Y. Luan, J. Jiang, Z. Kou, J. Wang, *Nanoscale* **2020**, *12*, 13225.

[24] S. K. Nataraj, K. S. Yang, T. M. Aminabhavi, *Prog. Polym. Sci.* **2012**, *37*, 487.

[25] M. S. A. Rahaman, A. F. Ismail, A. Mustafa, *Polym. Degrad. Stab.* **2007**, *92*, 1421.

[26] M. L. Minus, S. Kumar, *Jom* **2005**, *57*, 52.

[27] A. Moyseowicz, A. Śliwak, G. Gryglewicz, *J. Mater. Sci.* **2016**, *51*, 3431.

[28] D. Hulicova-Jurcakova, X. Li, Z. Zhu, R. de Marco, G. Q. Lu, *Energy and Fuels* **2008**, *22*, 4139.

[29] J. R. McDonough, J. W. Choi, Y. Yang, F. La Mantia, Y. Zhang, Y. Cui, *Appl. Phys. Lett.* **2009**, *95*, https://doi.org/10.1063/1.3273864.

[30] M. H. Al-Saleh, U. Sundararaj, *Carbon* **2009**, *47*, 2.

[31] W. Lu, M. Zu, J.-H. Byun, B.-S. Kim, T.-W. Chou, *Adv. Mater.* **2012**, *24*, 1805.

[32] A. S. Wu, T.-W. Chou, *Mater. Today* **2012**, *15*, 302.

[33] J. P. McGann, M. Zhong, E. K. Kim, S. Natesakhawat, M. Jaroniec, J. F. Whitacre, K. Matyjaszewski, T. Kowalewski, *Macromol. Chem. Phys.* **2012**, *213*, 1078.

[34] T. Liu, G. Liu, *J. Mater. Chem. A* **2019**, *7*, 23476.

[35] A. Álvarez-Gómez, J. Yuan, J. P. Fernández-Blázquez, V. San-Miguel, M. B. Serrano, *Polymers* **2022**, *14*, 5109.

[36] Y. Tan, D. Lin, C. Liu, W. Wang, L. Kang, F. Ran, *J. Mater. Res.* **2018**, *33*, 1120.

[37] R. D. Oliveira, C. S. Santos, J. R. Garcia, M. Vidotti, L. F. Marchesi, C. A. Pessoa, *J. Electroanal. Chem.* **2020**, *878*, 114662.

[38] D. Boonpakdee, C. F. Guajardo Yévenes, W. Surareungchai, C. La-O-Vorakiat, *J. Mater. Chem. A* **2018**, *6*, 7162.

[39] V. Vivier, M. E. Orazem, *Chem. Rev.* **2022**, *122*, 11131.

[40] H. D. Yoo, J. H. Jang, J. H. Ryu, Y. Park, S. M. Oh, *J. Power Sources* **2014**, *267*, 411.

[41] T. Q. Nguyen, C. Breitkopf, *J. Electrochem. Soc.* **2018**, *165*, E826.

[42] F. Lamberti, D. Ferraro, M. Giomo, N. Elvassore, *Electrochim. Acta* **2013**, *97*, 304.

[43] M. Crisci, F. Boll, L. Merola, J. J. Pflug, Z. Liu, J. Gallego, F. Lamberti, T. Gatti, *Front. Chem.* **2022**, *10*, 1.

[44] A. J. Bard, L. R. Faulkner, H. S. White, *Electrochemical Methods: Fundamentals and Applications*, Wiley-VCH Verlag, Hoboken, NJ **2000**.

[45] Q. Wu, T. He, Y. Zhang, J. Zhang, Z. Wang, Y. Liu, L. Zhao, Y. Wu, F. Ran, *J. Mater. Chem. A* **2021**, *9*, 24094.

[46] C. Hsiao, C. Lee, N. Tai, *J. Energy Storage* **2022**, *46*, 103805.

[47] L. Zhang, Y. Jiang, L. Wang, C. Zhang, S. Liu, *Electrochim. Acta* **2016**, *196*, 189.

[48] M. Shao, F. Ning, Y. Zhao, J. Zhao, M. Wei, D. G. Evans, X. Duan, *Chem. Mater.* **2012**, *24*, 1192.

[49] Z. Gao, J. Wang, Z. Li, W. Yang, B. Wang, M. Hou, Y. He, Q. Liu, T. Mann, P. Yang, M. Zhang, L. Liu, *Chem. Mater.* **2011**, *23*, 3509.

[50] Y. Zhai, Y. Dou, D. Zhao, P. F. Fulvio, R. T. Mayes, S. Dai, *Adv. Mater.* **2011**, *23*, 4828.

[51] H. Zhou, H. Chen, S. Luo, G. Lu, W. Wei, Y. Kuang, *J. Solid State Electrochem.* **2005**, *9*, 574.

[52] O. Norouzi, F. Di Maria, A. Dutta, *J. Energy Storage* **2020**, *29*, 101291.

[53] Q. Xu, H. Jiu, L. Zhang, W. Song, T. Gao, H. Wei, C. Wang, Y. Zhang, X. Li, *Ionics* **2022**, *28*, 1657.

[54] C. L. Chiang, J. M. Yang, *Flame Retardance and Thermal Stability of Polymer/Graphene Nanosheet Oxide Composites*, Elsevier Ltd, Amsterdam **2015**.

[55] M. Einert, C. Wessel, F. Badaczewski, T. Leichtweiß, C. Eufinger, J. Janek, J. Yuan, M. Antonietti, B. M. Smarsly, *Macromol. Chem. Phys.* **2015**, *216*, 1930.

[56] J. L. Hueso, J. P. Espinós, A. Caballero, J. Cotrino, A. R. González-Elipe, *Carbon* **2007**, *45*, 89.

[57] E. A. Arkhipova, A. S. Ivanov, N. E. Strokova, K. I. Maslakov, S. A. Chernyak, S. V. Savilov, *J. Therm. Anal. Calorim.* **2022**, *147*, 1081.

[58] B. Pollack, S. Holmberg, D. George, I. Tran, M. Madou, M. Ghazinejad, *Sensors* **2017**, *17*, 1.

[59] J. R. Pels, F. Kapteijn, J. A. Moulijn, Q. Zhu, K. M. Thomas, *Carbon* **1995**, *33*, 1641.

[60] L. Sun, C. Tian, Y. Fu, Y. Yang, J. Yin, L. Wang, H. Fu, *Chem. - A Eur. J.* **2014**, *20*, 564.

[61] A. C. Ferrari, *Solid State Commun.* **2007**, *143*, 47.

[62] C. Casiraghi, S. Pisana, K. S. Novoselov, A. K. Geim, A. C. Ferrari, *Appl. Phys. Lett.* **2007**, *91*, 1.

[63] A. Sadezky, H. Muckenhuber, H. Grothe, R. Niessner, U. Pöschl, *Carbon* **2005**, *43*, 1731.

[64] T. Jawhari, A. Roid, J. Casado, *Carbon* **1995**, *33*, 1561.

[65] X. Tian, X. Li, T. Yang, K. Wang, H. Wang, Y. Song, Z. Liu, Q. Guo, C. Chen, *Electrochim. Acta* **2017**, *247*, 1060.

[66] O. L. Li, S. Chiba, Y. Wada, G. Panomsuwan, T. Ishizaki, *J. Mater. Chem. A* **2017**, *5*, 2073.

[67] N. M. Keppetipola, M. Dissanayake, P. Dissanayake, B. Karunarathne, M. A. Dourges, D. Talaga, L. Servant, C. Olivier, T. Toupance, S. Uchida, K. Tennakone, G. R. A. Kumara, L. Cojocaru, *RSC Adv.* **2021**, *11*, 2854.

[68] X. B. Xie, D. Wu, H. Wu, C. Hou, X. Sun, Y. Zhang, R. Yu, S. Zhang, B. Wang, W. Du, *J. Mater. Sci. Mater. Electron.* **2020**, *31*, 18077.

[69] F. M. Hassan, V. Chabot, J. Li, B. K. Kim, L. Ricardez-Sandoval, A. Yu, *J. Mater. Chem. A* **2013**, *1*, 2904.

[70] A. C. M. Carvalho, M. C. Dos Santos, *J. Appl. Phys.* **2006**, *100*, https://doi.org/10.1063/1.2357646.

[71] Y. Liu, J. Zhou, L. Chen, P. Zhang, W. Fu, H. Zhao, Y. Ma, X. Pan, Z. Zhang, W. Han, E. Xie, *ACS Appl. Mater. Interfaces* **2015**, *7*, 23515.

[72] Z. Fan, J. Yan, T. Wei, L. Zhi, G. Ning, T. Li, F. Wei, *Adv. Funct. Mater.* **2011**, *21*, 2366.

[73] M. Sevilla, W. Sangchoom, N. Balahmar, A. B. Fuertes, R. Mokaya, *ACS Sustain. Chem. Eng.* **2016**, *4*, 4710.

[74] Q. P. Luo, L. Huang, X. Gao, Y. Cheng, B. Yao, Z. Hu, J. Wan, X. Xiao, J. Zhou, *Nanotechnology* **2015**, *26*, 304004.

[75] Z. Ling, Z. Wang, M. Zhang, C. Yu, G. Wang, Y. Dong, S. Liu, Y. Wang, J. Qiu, *Adv. Funct. Mater.* **2016**, *26*, 111.

[76] C. Chen, G. Xu, X. Wei, L. Yang, *J. Mater. Chem. A* **2016**, *4*, 9900.

[77] W. Na, J. Jun, J. W. Park, G. Lee, J. Jang, *J. Mater. Chem. A* **2017**, *5*, 17379.

[78] Z. Chen, K. Liu, S. Liu, L. Xia, J. Fu, X. Zhang, C. Zhang, B. Gao, *Electrochim. Acta* **2017**, *237*, 102.

[79] L. G. Cançado, K. Takai, T. Enoki, M. Endo, Y. A. Kim, H. Mizusaki, A. Jorio, L. N. Coelho, R. Magalhães-Paniago, M. A. Pimenta, *Appl. Phys. Lett.* **2006**, *88*, 1.

[80] H. G. J. Moseley, *Proc. R. Soc. A* **1913**, *88*, 471.

[81] J. I. Langford, A. J. C. Wilson, *J. Appl. Cryst.* **1977**, *11*, 102.

[82] E. Frank, F. Hermanutz, M. R. Buchmeiser, *Macromol. Mater. Eng.* **2012**, *297*, 493.